Quantitative retinal imaging with optical coherence tomography

Gräfe, M.G.O.

2020

document version
Publisher's PDF, also known as Version of record

Chapter 6 |

Subretinal Fibrosis Detection using Polarization Sensitive Optical Coherence Tomography

Abstract

Purpose: Subretinal fibrosis (SRFib) is an important cause of permanent loss of vision diseases with submacular neovascularization, but a reliable diagnostic method is currently missing. This study uses polarization-sensitive optical coherence tomography (PS-OCT) to detect SRFib within retinal lesions by measurement of its birefringent collagen fibers.

Methods: 25 patients were enrolled with retinal pathology in one or both eyes containing (1) suspected SRFib, (2) lesions suspected not to be fibrotic or (3) lesions with doubtful presence of SRFib. All eyes were evaluated for SRFIb using conventional diagnostics by three retinal specialists. PS-OCT images were visually evaluated for SRFib based on cumulative phase retardation, local birefringence and optic axis uniformity.

Results: 29 eyes from 22 patients were scanned successfully. In 13 eyes, SRFib was diagnosed by all retinal specialists, of these 12 were confirmed by PS-OCT and one was inconclusive. In nine eyes, the retinal specialists expected no SRFib, which was confirmed by PS-OCT in all cases. In seven eyes, the retinal specialists' evaluations were inconsistent with regard to the presence of SRFib. PS-OCT confirmed the presence of SRFib in four of these eyes, the absence of SRFib in two eyes, and was inconclusive in one eye.

Conclusion: In 21 out of 22 eyes, PS-OCT confirmed the evaluation of retinal specialists regarding the presence of SRFib. PS-OCT provided additional information to distinguish SRFib from other tissues within subretinal neovascular lesions in 6 out of 7 eyes.

Translational Relevance: PS-OCT can identify and quantify SRFib in doubtful cases for which a reliable diagnosis is currently lacking.

Based on: M. G. O. Gräfe*, J. A. van de Kreeke*, J. Willemse, B. Braaf, Y. de Jong, H. S. Tan, F. D. Verbraak, J. F. de Boer, "Subretinal Fibrosis Detection using Polarization Sensitive Optical Coherence Tomography", Translational Vision Science & Technology **9**, 13 (2020)

* these authors contributed equally to this work

6.1 Introduction

Age-related macular degeneration (AMD) with submacular neovascularizations is one of the most common causes of severe vision loss in the Western world [1, 2]. Recently, new treatments based on drugs suppressing vascular endothelial growth factor (anti-VEGF) have been developed to prevent severe vision loss in these patients [1, 3, 4]. However, even with anti-VEGF drug treatment, retinal tissue changes such as subretinal fibrosis (SRFib) can still develop in the course of submacular neovascularization, causing irreversible vision loss [5-7].

The development and presence of fibrosis is a prognostic factor for the future of visual acuity; therefore good imaging techniques to monitor the development of SRFib are therefore important for the selection of patients who may respond better (i.e. no fibrosis) or worse (i.e. mostly fibrotic lesions) to treatment [8]. Conventional imaging techniques such as fluorescein angiography (FA), indocyanine green angiography (ICGA), fundus photography and optical coherence tomography (OCT) give structural and circulatory information on retinal pathology [9-11]. However, none of these imaging techniques can reliably recognize and delineate fibrosis within retinal lesions. Fibrotic tissue can be suspected from highly reflective lesions on OCT in combination with visual acuity, fundus photography, FA and ICGA results [12] although a definitive diagnosis is still difficult.

OCT measures interferometrically the depth from which light is reflected within retinal structures [13]. Its main advantage over other techniques is that it not only measures a projected *en face* view of the retina, but also provides in-depth information for the creation of cross-sectional images. The importance of OCT in ophthalmology has increased enormously over the last years and OCT has become a standard tool for diagnostics and clinical research [14-16]. The recently developed OCT angiography is a promising new way to image retinal microvasculature and neovascular processes [17-19]. However, currently there is no standard method to reliably monitor the transition of non-fibrotic neovascular lesions into fibrotic neovascular lesions.

Birefringence is an optical property that changes the polarization state of the light, and manifests itself in fibrous tissues such as the retinal nerve fiber layer [20, 21]. Retinal nerve fiber layer birefringence has been used in the diagnosis and follow-up of glaucoma patients [22, 23]. Tissue birefringence alterations are also present during wound healing due to the changes in collagen and reticulin fiber structures [24]. Imaging methods that are sensitive to birefringence can therefore add an additional contrast modality to the existing techniques for improved detection of SRFib, which is a form of scar tissue consisting mostly of collagen fibers [6]. SRFib has therefore birefringent characteristics, allowing it to be visualized by polarization-sensitive OCT (PS-OCT) [25-27]. This makes PS-OCT a promising tool for reliable detection and three-dimensional delineation of fibrotic tissue within (sub)retinal lesions.

Shortly after the introduction of OCT, PS-OCT was developed [28, 29]. This functional form of OCT was shown to be able to detect the birefringent properties of collagen [29, 30] and later it was found that fibrotic tissue in the retina also provides significant contrast when examined with PS-OCT [26]. For an improved stability the PS-OCT bulk optics systems were further developed to fiber-based systems [31, 32]. Those systems came with new challenges, as the birefringence from the fiber components had to be separated from birefringence in the

sample [30]. It was shown that polarization mode dispersion (PMD) and other PS-OCT system distortions have to be corrected to obtain the most accurate results, which can be implemented based on Mueller [33] and Jones [34, 35] calculus. The latter was also applied in this study.

In this proof of concept study, we aimed to use PS-OCT for finding and delineating SRFib in subretinal neovascular pathology, most notably neovascular AMD.

6.2 Methods

6.2.1 Participants

25 patients of the Amsterdam UMC, location VUmc were enrolled for scanning with the PS-OCT. The study followed the tenets of the Declaration of Helsinki and written informed consent was obtained from all patients. The study was approved by the Medical Ethics Committee of the Amsterdam UMC, location VUmc in Amsterdam. Patients were included if they had macular lesions. Two patients had fibrosis caused by multifocal choroiditis with inflammatory choroidal neovascularization (CNV) and three had myopic/idiopathic CNV. All other patients had neovascular AMD. The macular lesions were sorted into three categories: (1) neovascular lesions with suspected fibrosis, (2) lesions suspected to consist of material not of fibrotic origin or (3) neovascular lesions in which there was doubt as to whether they contained fibrosis. The lesions judged as fibrotic (N=13) were fibrotic scars: one was quiet and had not been under anti-VEGF-treatment for several years, and five had not received anti-VEGF treatment due to long existence. The remaining lesions judged as fibrosis (N=7) were type 2 (classic) CNVs, partially fibrotic but still under anti-VEGF treatment. A definition when fibrosis was suspected based on examinations is given below. From the group of eyes with lesions suspected not to contain fibrotic material (N=9), five were type 1 CNVs with fibrovascular pigment epithelial detachment (PED) and were under anti-VEGF-treatment. The remaining four eyes of two patients in this group had pseudovitelliform macular lesions, one of these patients (i.e. two eyes) had received anti-VEGF earlier, and the other patient had not. Lesions without suspected fibrosis were chosen as negative controls. Some of both of the type 1 and type 2 CNVs were judged as doubtful (N=7). Exclusion criteria were severe media opacity hindering retinal imaging or inability to acquire reliable images. Demographic data about the study population are included in Table 6.1.

6.2.2 Examinations

Best corrected visual acuity (BCVA), slit lamp biomicroscopy and OCT (Spectralis, Heidelberg Engineering GmbH) were obtained for all patients as part of standard care. PS-OCT was obtained successively after their usual check-up, so all examinations were performed on the same day. All eyes were dilated with tropicamide 0.5% and phenylephrine 5% prior to imaging. Fundus photography (45-50 degrees, Topcon Corp.) of the region of interest was obtained for the eyes scanned with PS-OCT.

Table 6.1. Demographics of the study population. Values are means unless indicated otherwise. * This value was averaged over all eyes instead of participants. BCVA = Best Corrected Visual Acuity. CNV = choroidal neovascularization.

Demographic	**Value**
Number of participants (N)	22
Number of eyes (N)	29
Sex, female N (%)	12 (54.5%)
Age (years), mean ± SD	75.0 (±14.0)
BCVA (LogMAR)*, mean ± SD	0.69 (±0.65)
Diagnosis	
- Neovascular AMD (N eyes,%)	24 (82.8%)
- Myopic/idiopathic CNVs (N eyes, %)	3 (10.3%)
- Multifocal choroiditis (N eyes, %)	2 (6.9%)

6.2.3 Defining fibrosis

All eyes were judged by three retinal specialists to make a prediction on whether fibrosis was expected. Eyes where the three specialists were inconsistent or inconclusive in their judgment were marked as 'doubtful fibrosis'. To make an evaluation regarding the presence of fibrosis, the specialists based their judgement on BCVA, OCT images and fundus photography of the included eye. SRFib was defined as a yellow-whitish lesion on fundoscopy and fundus photography, and as a hyperreflective lesion on OCT at the level of the Retinal Pigment Epithelium (RPE) combined with low BCVA when the lesion was subfoveal in accordance with earlier definitions [12]. The presence of fibrosis using the PS-OCT was defined by visual inspection of the images and criteria described in section 6.2.5 Processing & evaluation.

6.2.4 Polarization-sensitive optical coherence tomography

The PS-OCT imaging system was introduced in Braaf *et al.* [35] and modifications to improve the A-line phase stability have been described in Gräfe *et al.* [36]. In short, light from a swept-source (Axsun Technologies Inc.) with a 1060 nm central wavelength was inserted into a single-mode, fiber-based OCT interferometer. In the sample arm the light was split into two orthogonal polarization states, and one state was delayed in time before it was sent into the eye. The time delay caused a shift in depth between the two states in the OCT image, which allowed for their individual detection (depth-multiplexing). After recombination with the reference arm the OCT light was split into two orthogonal polarization channels and recorded through balanced detection. The depth-multiplexed images were acquired with 1536 samples per A-line, 2000 A-lines per B-scan and 300 B-scans of an area of 6-by-6 mm. The acquisition time for one C-scan was 6.6 s. The axial resolution of the PS-OCT system was 8.7 μm (in air), and the beam diameter at the cornea was 1.1 mm. A fixation target was presented to the contralateral eye.

6.2.5 Processing & evaluation

Initial OCT processing steps were signal roll-off compensation [35], fixed pattern removal [37] spectral shaping by a tapered cosine window and digital chromatic dispersion compensation [38]. In the supplementary material the overlay between the depth-delayed polarization states

and the compensation for polarization mode dispersion (PMD) is described. OCT intensity images were computed by coherent signal composition [39]. Images of three PS-OCT contrast modalities were used to identify birefringent fibrotic areas in tissue: cumulative double-pass phase retardation (DPPR) [30, 35], local birefringence [40], and optic axis uniformity (OAxU) [41-43]. The cumulative DPPR measures the phase retardation between the principle polarization states along the complete optical path through the tissue. When deeper locations are measured within birefringent tissues the optical path becomes longer, and more cumulative DPPR will be measured until reaching a value of π from which it decreases again due to phase wrapping. An increasing slope is characteristic for cumulative DPPR in birefringent structures (until π). In contrast, the local birefringence is a measure of the phase retardation effect at a single depth location and does not accumulate with longer optical paths. The local birefringence is proportional to the amount of actual birefringent material (with optic axis perpendicular to the incident light) per pixel in the OCT image [40]. Local birefringence images show high signal at the locations of high concentration of birefringent tissue. In general images of the cumulative DPPR are used for sensitive qualitative evaluation of the birefringence in the retina, whereas the local birefringence gives quantitative information but with lower sensitivity. In many biological tissues the orientation of fiber bundles can be measured from the optic axis of the birefringent fibrous tissue. The OAxU uses this property to indicate areas with significant concentration of highly aligned fibers. OAxU combines similar sensitivity of cumulative DPPR and the axial localization of local birefringence and can therefore only be used for binary decisions and not for quantification.

Visual inspection included inspection of images from above mentioned contrast modalities with two members of the research team (MGOG, JAvdK). If no consensus was reached, a retinal specialist (FDV) was consulted as final judge. Images were judged positive for birefringence if a clear and consistent elevated level of local birefringence was present in multiple adjacent B-scans and the OAxU was high in the same areas. In some scans local birefringence was not significantly elevated but OAxU could still reveal a good birefringent contrast. In those cases the cumulative DPPR was used to make a final judgement. Expected high birefringence contrast from scleral tissue and the retinal nerve fiber layer (RNFL) were ignored. Certain scans showed regions with high local birefringence with a speckled, highly fluctuating behavior, low OAxU and strong attenuation (the signal-to-noise ratio, SNR, was weak below these regions, so cumulative DPPR could not be used). Those effects could be attributed to depolarization by a local accumulation of pigment as seen on the corresponding fundus photograph, as the presence of melanin pigments was shown not only to be strongly attenuating but also depolarizing [44-46]. Those areas were excluded and not considered to be fibrotic.

6.3 Results

25 patients were enrolled in the study. In three patients, scanning failed due to technical failure (N=2) or inability to make a reliable image (N=1). A total of 29 eyes from 22 patients were scanned successfully with the PS-OCT system. 24 eyes had a diagnosis of neovascular AMD and five had other diagnoses: myopic/idiopathic CNV (N=3) and multifocal choroiditis

(N=2). The panel of three specialists judged 13 out of 29 eyes to have SRFib and nine to be negative for SRFib; they were in disagreement or in doubt about seven eyes. Visual inspection using PS-OCT scans revealed 16 scans to be positive for birefringence within the lesion (i.e. to contain fibrosis) and 11 were negative; in two a definite diagnosis could not be made. Table 6.2 shows the matching between retinal specialists using conventional diagnostics and the diagnostics based on the criteria described in 6.2.5 Processing & evaluation for PS-OCT scans.

Table 6.2. The judgement on the presence of subretinal fibrosis in 29 eyes by three retinal specialists using conventional diagnostics (i.e. fundus images, OCT and BCVA) versus presence of elevated birefringence (i.e. fibrosis) by visual inspection on polarization sensitive optical coherence tomography (PS-OCT). (PS)OCT = (Polarization Sensitive) Optical Coherence Tomography, BCVA = Best Corrected Visual Acuity.

Clinical assessment (fundus images, OCT and BCVA)	Fibrosis on PS-OCT	No fibrosis on PS-OCT	Inconclusive on PS-OCT	**Total**
Suspected fibrosis	12	0	1	**13**
No suspected fibrosis	0	9	0	**9**
In doubt	4	2	1	**7**
Total	**16**	**11**	**2**	**29**

SRFib was suspected by the retinal specialists in 13 eyes and PS-OCT confirmed 12 of these cases by showing an elevated birefringent signal and high optic axis uniformity within the lesions. In the remaining case with suspected fibrosis, the PS-OCT images were deemed inconclusive. In this case high myopia and a resulting thin retina caused significant birefringence/optic axis uniformity from the scleral tissue obscuring a potential signal from fibrotic tissue. Fig. 6.1 shows example images for one of the 12 positive cases of patients with suspected SRFib where PS-OCT scans confirmed its presence. The birefringent region can clearly be identified. Local birefringence and OAxU provide strong contrast for the areas of fibrotic tissue. The signals in cumulative phase retardation supports this. The fibrotic material highlighted by PS-OCT is located within the hyperreflective layer (dark layer in structural image). It corresponds to the region / where yellow material can be found in the fundus image but it has a distinct substructure. The refractive index difference that corresponds to the maximum of the displayed local birefringence is $\Delta n=2.04\cdot10^{-3}$. This is a range similar to what was reported for collagen in scar tissue in skin [47] ($1.55\cdot10^{-3}$), tendon [48] ($3.0\cdot10^{-3}$), stroma around malignant lesions in breast tissue [40] ($2.2\cdot10^{-3}$) or chicken muscle [32] ($2.3\cdot10^{-3}$). Because of the good contrast-to-noise ratio, as shown by Willemse *et al.* [43], it was possible to choose a lower bound for the OAxU images (0.70) above the noise floor in tissue (0.55) with a maximum of 1.00.

The next case is an example of SRFib when the fibrotic tissue was on the more difficult end of being identifiable by the images created from PS-OCT data. In this case not all modalities would lead to the same conclusion regarding the presence of birefringence. In some cases, the cumulative DPPR was clearly positive for birefringence, whereas this was not as pronounced or was even absent in the local birefringence images. Fig. 6.2 shows an example of a birefringent signal present in the cumulative DPPR image, but absent in the local

birefringence image. The OAxU image shows higher sensitivity to the weak birefringent structures than the local birefringence but with similar spatial confines. OAxU images were often able to give conclusive evidence on the presence or absence of birefringent tissue in such cases, as fibers causing birefringence are oriented in the same direction (within the corresponding kernel), which results in a high optic axis uniformity.

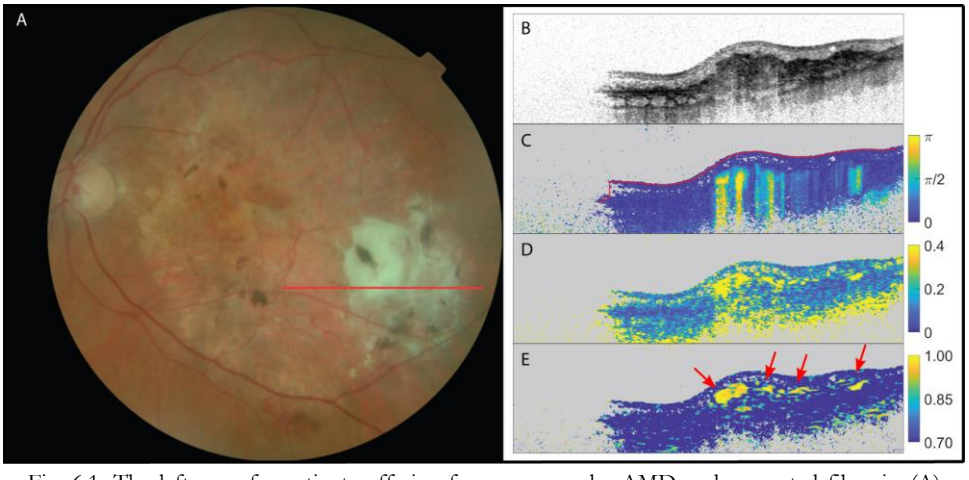

Fig. 6.1. The left eye of a patient suffering from neovascular AMD and suspected fibrosis. (A) fundus image, (B) OCT intensity image (colorscale: 0-33 dB), (C) cumulative retardation image (in rad), (D) local birefringence image (in °/μm), the upper limit (0.4 °/μm) corresponds to a refractive index difference of $\Delta n=2.04 \cdot 10^{-3}$; and (E) optic axis uniformity image. Note the elevated birefringent signal in scans (C) and (D) as well as the high optic axis uniformity in (E) on PS-OCT images, confirming the presence of SRFib. The red arrows point at fibrotic structures. Signal on the left side of images is missing due to beam clipping.

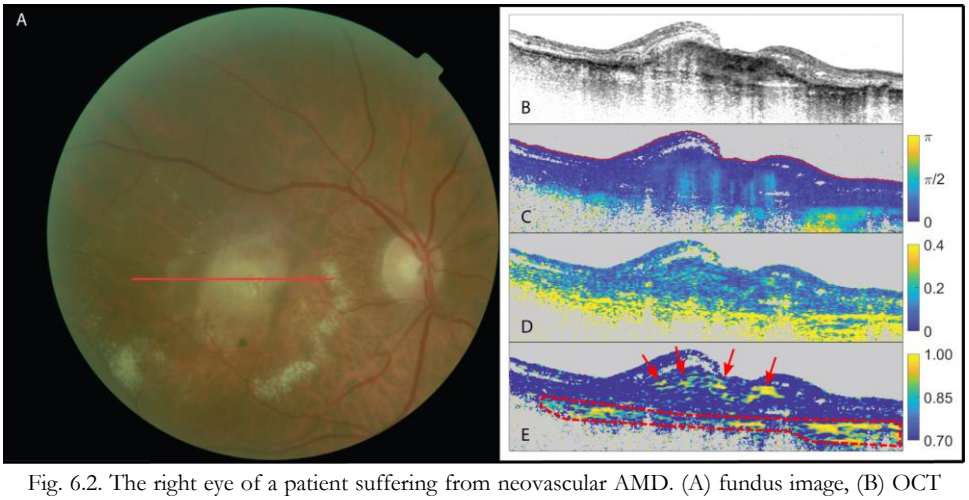

Fig. 6.2. The right eye of a patient suffering from neovascular AMD. (A) fundus image, (B) OCT intensity image (colorscale: 0-33 dB); (C) cumulative retardation image (in rad); (D) local birefringence image (in °/μm); and (E) optic axis uniformity image. Note the presence of birefringent signal in the cumulative phase retardation on scan (C) and its absence in the local phase retardation on scan (D) in the PS-OCT images. A high optic axis uniformity signal on scan (E)

confirms the presence of birefringent tissue in this case. The red arrows point at fibrotic tissue. Scleral tissue was delineated with a red dashed line.

In a total of nine eyes, the retinal specialists expected no subretinal fibrosis. All nine cases were confirmed by PS-OCT, as neither a birefringent signal nor optic axis uniformity was present. Fig. 6.3 shows the images of a patient with no suspected fibrosis and PS-OCT confirming this absence of fibrosis.

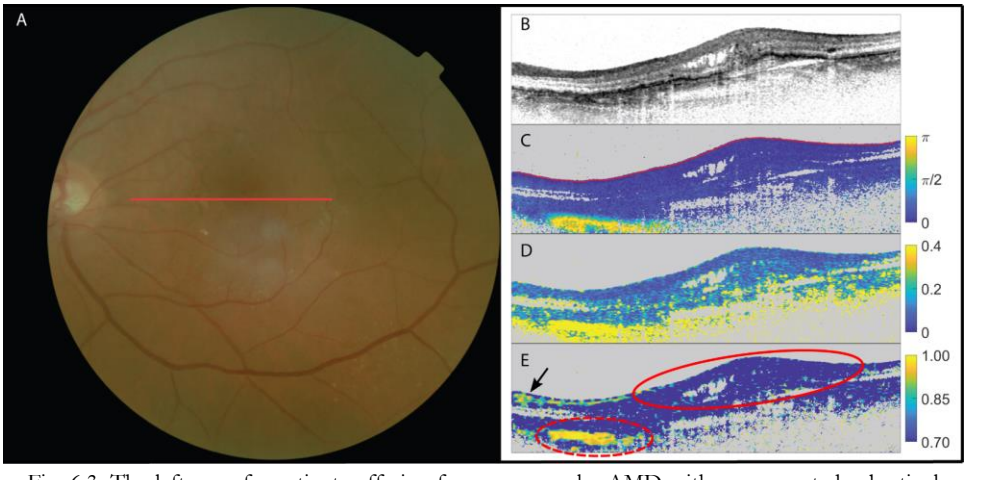

Fig. 6.3. The left eye of a patient suffering from neovascular AMD with no suspected subretinal fibrosis. **(**A) fundus image; (B) OCT intensity image (colorscale: 0-33 dB); (C) cumulative retardation image (in rad), (D) local birefringence image (in °/μm), (E) optic axis uniformity image. Note the absence of significant birefringent signal in the lesion in scans (C) and (D) as well as the lack of optic axis uniformity in (E) in the PS-OCT images, confirming the absence of fibrosis within this lesion (delineated with red solid line). The elevated birefringence in the lower nasal side (delineated with red dashed line) on the scans signifies the sclera (which is also highly birefringent with a resulting high optic axis uniformity). High signal in OAxU from RNFL is indicated by a black arrow.

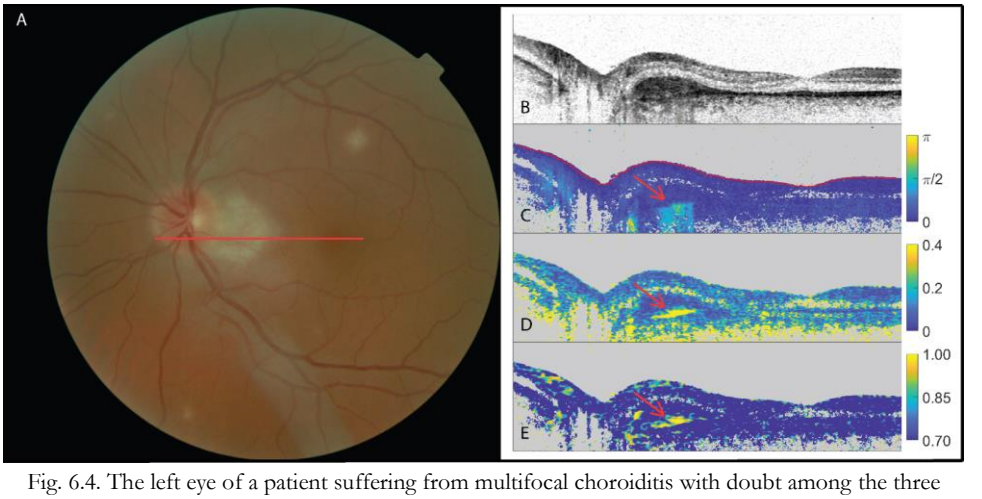

Fig. 6.4. The left eye of a patient suffering from multifocal choroiditis with doubt among the three retinal specialists (two positive, one negative) as to the presence of subretinal fibrosis. (A) Fundus

image; (B) OCT intensity image (colorscale: 0-33 dB); (C) cumulative retardation image (in rad); (D) local birefringence image (in °/μm); (E) optic axis uniformity image. Scleral tissue was delineated with red dashed lines. High signal in OAxU was indicated by a black arrow. Note the elevated birefringent signal in scans (C) and (D) and high optic axis uniformity in (E) in the PS-OCT images (red arrows), indicating the presence of fibrosis.In a total of seven eyes, the retinal specialists were either in doubt or in disagreement on the presence of subretinal fibrosis. Of these seven eyes, PS-OCT showed a birefringent signal and high optic axis uniformity in four, signifying the presence of fibrosis, and neither a birefringent signal nor optic axis uniformity in two eyes, signifying the absence of fibrosis.

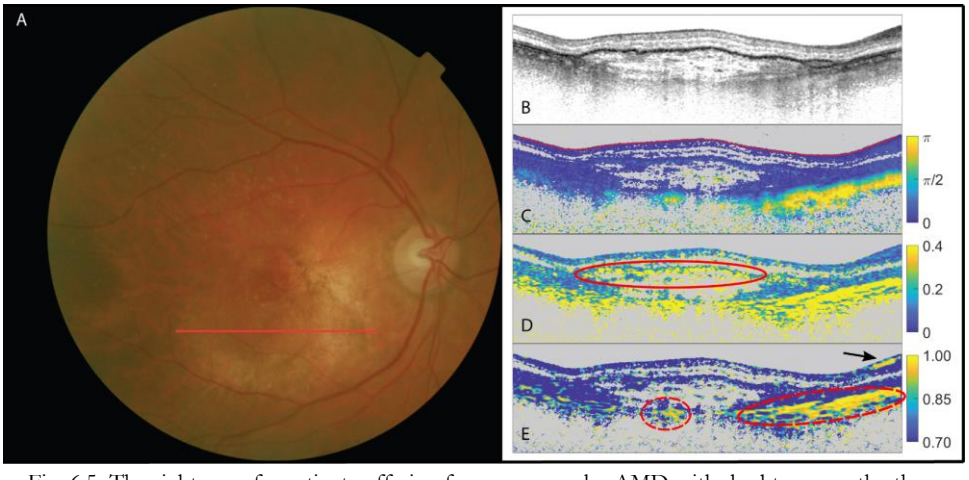

Fig. 6.5. The right eye of a patient suffering from neovascular AMD with doubt among the three retinal specialists as to the presence of subretinal fibrosis. (A) fundus image: (B) OCT intensity image (colorscale: 0-33 dB); (C) cumulative retardation image (in rad); (D) local birefringence image (in °/μm), where the speckled, highly fluctuating behavior (delineated with a solid red line) was attributed to depolarization due to stronger pigmentation; and (E) optic axis uniformity image. Despite the local birefringence showing significant signal the scan was judged negative, because neither OAxU nor cumulative birefringence support the indication by local birefringence. The elevated birefringence in the lower right part on the scans signifies the sclera (which is also highly birefringent with a resulting high optic axis uniformity).

In one eye, the PS-OCT scan was deemed inconclusive due to the low quality of the scan and the resulting low signal-to-noise ratio. Fig. 6.4 and 6.5 show examples of these seven eyes. Although elevated birefringence and high optic axis uniformity were found that indicated SRFib as shown in Fig. 6.4, the same could not be identified in the case presented in Fig. 6.5.

Based on PS-OCT data a two-dimensional *en face* projection can be created. As a first example, Fig. 6.6 shows the *en face* image of the same patient as shown in Fig. 6.1. A volume of 100 pixels (≈ 400 μm) below the inner limiting membrane (ILM) was chosen from one data set and the median of the cumulative DPPR along the A-scans was used for the projection, which in this particular case approximately included the RPE but excluded the sclera. The fibrotic lesion was highlighted by OAxU and the intensity en face image where more than 30% of the segmented pixels had an OAxU value of 0.70 or higher. The heterogeneous distribution of fibrosis within the lesion can be appreciated in Fig. 6.6C

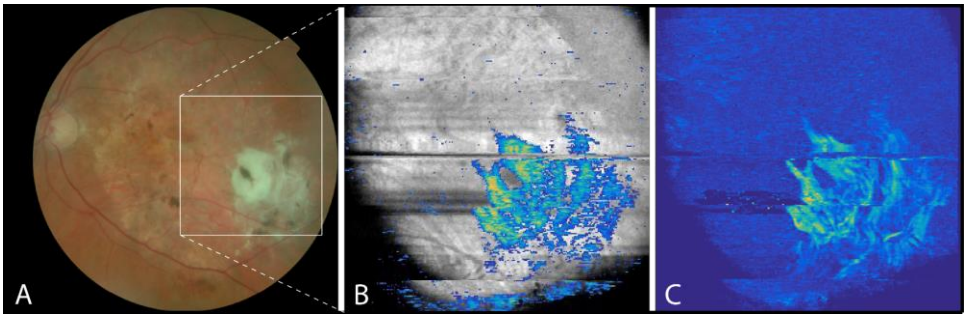

Fig. 6.6 En face views of the left eye of a patient suffering from neovascular AMD and suspected fibrosis. (A) fundus image; (B) overlay of en face OCT intensity image with scar highlighted by OAxU; and (C) en face phase retardation image. Note the birefringent signal in parts of the lesion in scan C, delineating the heterogeneous presence of fibrosis within the lesion. A movie of the B-scans of the volume of (B) can be viewed in the supplementary material of the journal article.

6.4 Discussion

In this proof-of-concept study, we have demonstrated the diagnostic capabilities of PS-OCT in finding and delineating subretinal fibrosis in retinal neovascular pathology. We successfully scanned 29 eyes with retinal pathology using PS-OCT, and in 27 of them the presence or absence of fibrosis was concluded.

There is currently no gold standard for detecting subretinal fibrosis in retinal lesions. The presence of fibrosis can be suspected by retinal specialists with the evaluation of fundus images or conventional OCT scans, in combination with clinical information such as visual acuity [12]. In some instances however, the presence or absence of fibrosis is very difficult to define for retinal specialists, as lesions may be very heterogenic. This study illustrates this problem, as in seven out of 29 eyes the retinal specialists could not reach consensus of the presence of SRFib (Table 5.1). PS-OCT makes use of the birefringent properties of fibrosis to establish its presence, offering an additional and potentially more reliable detection method [25, 26].

In most cases with a birefringent signal, the fibrotic lesions showed a spatially heterogeneous patchy structure rather than a uniform birefringent layer. Those correlate with the occurrence of yellow-whitish lesions in the fundus images and formation of a hyperreflective layer in the structural images (in clear cases) but show more details of the local distribution of fibrotic tissue. In cases which were graded doubtful by the retinal specialists but positive on PS-OCT, birefringent material could be found even if yellow-whitish lesions were not recognized by the retinal specialists. Thus, these patterns do not match exactly and, especially in doubtful cases, can lead to misinterpretations. The occurrence of the patchy structures is similar to what has been reported earlier by Roberts *et al.* [26] and could reflect an irregular pattern of inflammation and healing processes. The development of subretinal fibrosis is similar to that of fibrosis in other parts of the body; tissue inflammation causes the release of mediators recruiting inflammatory cells and fibroblasts. Neovascularization triggers a similar process, and especially after repeated injury/inflammation a fibrotic scar will remain [6]. This scarring is then likely to resemble the local inflammation and neovascularization [49].

The three image modalities, cumulative DPPR, local birefringence and OAxU, can

together be used in complementary ways due to their different advantages and disadvantages. Cumulative DPPR and OAxU were more sensitive to recognizing weak birefringent structures. This was particularly helpful in doubtful cases: if fibrosis could not be found with the local birefringence signal but OAxU showed high signal and it could be confirmed with cumulative DPPR, then it was still judged positive. In Fig. 6.2C a moderate increase of DPPR above the noise floor can be seen whereas hardly any signal changes can be recognized in 6.2D. OAxU shows again a significant signal in an area that could be attributed to the existence of fibrotic tissue. In addition to its good sensitivity to low birefringence, OAxU can also be applied for axial localization of birefringent structures. Despite their good sensitivity, OAxU and cumulative DPPR could only be used for binary decisions whether fibrotic tissue is present or not. Local birefringence calculation, on the other hand, offers potential for the quantification of birefringent tissue [40].

Including the local contrast modes (OAxU [41-43] and local birefringence [40]) in addition to cumulative DPPR as published in previous work [20, 26, 27, 50] allowed better evaluation of the extent of fibrotic lesions in depth and made the judgement regarding the presence of SRFib more reliable. OAxU and local birefringence are also more convenient to use: cumulative DPPR images are in general harder to interpret for clinicians due to their shadow-like artifacts below the actual birefringent material whereas the axial confinement of local birefringence and OAxU offers a more intuitive way of displaying and judging results.

In addition to structural and birefringence images of B-scans and the diagnosis of fibrosis with the above-mentioned criteria, the PS-OCT data can also be applied to *en face* projections such as shown in Fig. 6.6 to help mapping out the extend of fibrotic lesions and provide additional value for clinical diagnostics. En face images of the fibrotic lesion can be created, provided that the birefringent signals from RNFL and sclera are excluded from the projection. In Fig. 6.6 a projection depth was chosen which included the signal from the fibrotic tissue but excluded the sclera. The birefringent signal in the RNFL is weaker and in this example completely dominated by the signal from the fibrotic tissue. To standardize this method, a robust segmentation is required to exclude scleral tissue as it can for example be seen in the lower right part of Fig. 6.5C. If weak signals are to be analyzed (especially for quantitative analysis) such as in Fig. 5.2, segmentation and exclusion of the RNFL might also be necessary.

In conclusion, this study has shown that PS-OCT, and especially the local birefringence and OAxU, provide a novel contrast mechanism for detecting subretinal fibrosis within retinal neovascular lesions. There was a high agreement among the evaluation of the three retinal specialists regarding the presence of SRFib and a birefringent signal in combination with high OAxU within a lesion when using PS-OCT. In cases where the retinal specialists were in disagreement or decisions were inconclusive, PS-OCT could provide additional information to guide the diagnosis. PS-OCT could be used to evaluate how fibrotic scars within the retina develop over time by monitoring patients over the course of several months or years. This can provide invaluable insight into the development of SRFib in the presence of a CNV and to contribute to investigating the effects of various treatment options on the development of fibrosis. Furthermore, PS-OCT can be a very interesting tool for quantification of birefringence and might also be of interest for the investigation of other pathologies such as glaucoma, that affect the disease the RNFL tissue and the embedded birefringent nerve fibers.

6.5 Supplementary Material

In the following section complementary details on the in-house built polarization sensitive OCT system and its improved post-processing of the acquired data specifically designed for this study, are described.

6.5.1 Overlay of the depth multiplexed polarization state images

In order to determine the birefringence parameters of a sample, the sample is probed with two orthogonal polarization states and in the detection the signal is split into two orthogonal detection channels. The different input states are created in a polarization delay unit where, after being separated by a polarization beam splitter, the states are delayed in time before being sent to the sample (the retina). The time delay between the different input polarization states creates a depth displacement between their images. During the PS-OCT data processing this displacement needs to be determined and compensated. The depth displacement calculation was done by computing the autocorrelation from the Fourier transform of the squared real valued OCT signal in spectral domain: $AC = FFT\{S(k)^2\}$. The autocorrelation was averaged over a full B-scan yielding a clear peak representing the displacement between the input polarization states. Sub-pixel accuracy was achieved by computing the center of mass of the autocorrelation peak p. To compensate this depth delay, the image of the delayed polarization state was shifted to the same depth position as the image from the non-delayed polarization state by applying a complex phase ramp to the spectral domain signal: $S(k) \cdot \exp[i2\pi \cdot p/n]$ with n the index number of the wavenumber samples.

6.5.2 PS-OCT post-processing improvements

The correction of system polarization distortions including PMD of the PS-OCT measurements has been described previously [35]. Here improvements for an automated judgement on the quality of the correction functions are described for a more robust use in clinical practice. Correction functions were determined across 15 spectral bins. Automated feedback of the correction was used to help the user choose an optimal B-scan from which the corrections could be computed and was based on criteria described subsequently. In order to eliminate polarization distortions in the optical path from the retina to the detector, the surface polarization state at the vitreous humor-retina interface must be determined. It has been found that the detection of the interface is more robust if the degree of polarization uniformity (DOPU)[44] from uncorrected data is used in comparison to intensity images. In addition, areas where the signal is weak (e.g. by beam clipping) were excluded from surface state detection through thresholding of the skewness of the distribution of intensity data of the A-lines. The skewness was found to be a good indicator whether a signal was recorded which can be discriminated from the noise floor. Next, a sufficient amount of pixels with significant phase retardation (>0.1 rad) is necessary to build up statistical ensembles to determine the correction functions for the remaining system distortions. It has been found empirically that pixel numbers above 20 000 suffice and thus, neighboring B-scans are included in the ensemble if less pixels are counted in a single B-scan. The correction functions are extracted from the eigenvector elements for each pixel which can be described as [35]:

$$v(k)=\begin{bmatrix} v_{11} & v_{12} \\ v_{21} & v_{22} \end{bmatrix}=\begin{bmatrix} \alpha(k)\cdot e^{i(k\gamma'+\rho(k))} & 0 \\ 0 & 1 \end{bmatrix}^{-1}\begin{bmatrix} x(k) & -y(k)^* \\ y(k) & x(k)^* \end{bmatrix}\begin{bmatrix} s_1 & 0 \\ 0 & s_2 \end{bmatrix} \quad (6.1)$$

where $\alpha(k)$ is the amplitude ratio between the two input states, k the wavenumber, γ' the residual displacement after overlap of the depth-multiplexed images, $\rho(k)$ the phase difference between vertical and horizontal field components before the PDU, $[x(k), -y(k)^*; y(k), x(k)^*]$ is a Unitarian matrix including the incoming path and a standard rotation matrix, and s_1 and s_2 are complex scalars needed for eigenvector normalization. Eq. (6.1) was used to determine $\alpha(k)$ and the amplitudes of s_1, s_2, $x(k)$ and $y(k)$ using histograms of the amplitudes of the eigenvector components under the assumption that each is represented by a monomodal distribution where the maximum reflects the expectation value. Depending on the selected B-scan it can deviate from this ideal case, e.g. if the relative optical axis orientations are diverse and induce multimodal distributions. This effect is checked by a fit of a Gaussian distribution to the histograms and the R^2 values are computed for those fits and displayed to the user. It was found empirically that R^2 values above 0.95 indicated that the histograms from the selected B-scan(s) could be considered monomodal distributions and that they were suitable for a robust determination of the correction parameters. In addition the phase functions $\varphi_v(k)=\arg\left(x(k)\cdot y(k)\cdot e^{-i(k\gamma'+\rho(k))}\right)$ and $\varphi_{XY}(k)=\arg\left(x(k)\cdot y(k)\right)$ were determined. For physically meaningful results those functions should only show low to moderate oscillations across the spectrum, which was checked with the tortuosity parameter $T=L/C$ with the length L of the curve and the distance C between first and last point. If T was below a value of 2 the correction functions were found to be reliable. These criteria were used to choose a suitable B-scan for the calibration of the polarization distortion compensation which was then applied to all B-scans in a full volume.

6.5.3 Visualization of local birefringence

The visualization of local birefringence was implemented according to Villiger *et al.* [40] in which the original measurements in the Jones space are converted to Mueller space. In this method spatial averaging (3 in depth by 7 lateral pixels $\hat{=}$ 16.2 μm by 21 μm) of the Mueller matrices was used and birefringent parameters were extracted from the differential Mueller matrices over one pixel in depth (5.4 μm in air) and converted to a birefringence vector. This vector was averaged with a second spatial filter of 10 by 20 pixels. For OAxU [42, 43] calculation a two-dimensional kernel of 10 by 20 pixels was used.

Funding

This work has received support from Oogfonds Nederland, Algemene Nederlandse Vereniging ter Voorkoming van Blindheid (ANVVB) (www.uitzicht.nl) and from the Dutch Technology Foundation STW (grant number 12822), which is part of the Netherlands Organisation for Scientific Research (NWO)

References

1. L. S. Lim, P. Mitchell, J. M. Seddon, F. G. Holz, and T. Y. Wong, "Age-related macular degeneration," Lancet **379**, 1728-1738 (2012).
2. A. L. Pelletier, L. Rojas-Roldan, and J. Coffin, "Vision Loss in Older Adults," Am Fam Physician **94**, 219-226 (2016).
3. S. D. Solomon, K. Lindsley, S. S. Vedula, M. G. Krzystolik, and B. S. Hawkins, "Anti-vascular endothelial growth factor for neovascular age-related macular degeneration," Cochrane Database Syst Rev, CD005139 (2014).
4. C. L. Nguyen, L. J. Oh, E. Wong, J. Wei, and M. Chilov, "Anti-vascular endothelial growth factor for neovascular age-related macular degeneration: a meta-analysis of randomized controlled trials," BMC Ophthalmol **18**, 130 (2018).
5. J. C. Hwang, L. V. Del Priore, K. B. Freund, S. Chang, and R. Iranmanesh, "Development of subretinal fibrosis after anti-VEGF treatment in neovascular age-related macular degeneration," Ophthalmic Surg Lasers Imaging **42**, 6-11 (2011).
6. K. Ishikawa, R. Kannan, and D. R. Hinton, "Molecular mechanisms of subretinal fibrosis in age-related macular degeneration," Exp Eye Res **142**, 19-25 (2016).
7. E. Daniel, C. A. Toth, J. E. Grunwald, G. J. Jaffe, D. F. Martin, S. L. Fine, J. Huang, G. S. Ying, S. A. Hagstrom, K. Winter, M. G. Maguire, and G. Comparison of Age-related Macular Degeneration Treatments Trials Research, "Risk of scar in the comparison of age-related macular degeneration treatments trials," Ophthalmology **121**, 656-666 (2014).
8. A. C. Pedrosa, T. Sousa, J. Pinheiro-Costa, J. Beato, M. S. Falcao, F. Falcao-Reis, and A. Carneiro, "Treatment of Neovascular Age-Related Macular Degeneration with Anti-VEGF Agents: Predictive Factors of Long-Term Visual Outcomes," J Ophthalmol **2017**, 4263017 (2017).
9. U. Schmidt-Erfurth, S. Klimscha, S. M. Waldstein, and H. Bogunovic, "A view of the current and future role of optical coherence tomography in the management of age-related macular degeneration," Eye (Lond) **31**, 26-44 (2017).
10. M. M. Castillo, G. Mowatt, A. Elders, N. Lois, C. Fraser, R. Hernandez, W. Amoaku, J. M. Burr, A. Lotery, C. R. Ramsay, and A. Azuara-Blanco, "Optical coherence tomography for the monitoring of neovascular age-related macular degeneration: a systematic review," Ophthalmology **122**, 399-406 (2015).
11. A. J. Gess, A. E. Fung, and J. G. Rodriguez, "Imaging in Neovascular Age-Related Macular Degeneration," Seminars in Ophthalmology **26**, 225-233 (2011).
12. A. S. Willoughby, G. S. Ying, C. A. Toth, M. G. Maguire, R. E. Burns, J. E. Grunwald, E. Daniel, G. J. Jaffe, and G. Comparison of Age-Related Macular Degeneration Treatments Trials Research, "Subretinal Hyperreflective Material in the Comparison of Age-Related Macular Degeneration Treatments Trials," Ophthalmology **122**, 1846-1853 e1845 (2015).
13. D. Huang, E. A. Swanson, C. P. Lin, J. S. Schuman, W. G. Stinson, W. Chang, M. R. Hee, T. Flotte, K. Gregory, C. A. Puliafito, and J. G. Fujimoto, "Optical Coherence Tomography," Science **254**, 1178-1181 (1991).
14. S. R. Sadda, "Defining the Role of OCT Angiography in Clinical Practice," Ophthalmology Retina **1**, 261-262 (2017).
15. R. Daneshvar and K. Nouri-Mahdavi, "Optical Coherence Tomography Angiography: A New Tool in Glaucoma Diagnostics and Research," J Ophthalmic Vis Res **12**, 325-332 (2017).
16. M. Adhi and J. S. Duker, "Optical coherence tomography--current and future applications," Curr Opin Ophthalmol **24**, 213-221 (2013).

17. N. V. Palejwala, Y. L. Jia, S. S. Gao, L. Liu, C. J. Flaxel, T. S. Hwang, A. K. Lauer, D. J. Wilson, D. Huang, and S. T. Bailey, "Detection of Nonexudative Choroidal Neovascularization in Age-Related Macular Degeneration with Optical Coherence Tomography Angiography," Retina-J Ret Vit Dis **35**, 2204-2211 (2015).
18. Y. L. Jia, S. T. Bailey, D. J. Wilson, O. Tan, M. L. Klein, C. J. Flaxel, B. Potsaid, J. J. Liu, C. D. Lu, M. F. Kraus, J. G. Fujimoto, and D. Huang, "Quantitative Optical Coherence Tomography Angiography of Choroidal Neovascularization in Age-Related Macular Degeneration," Ophthalmology **121**, 1435-1444 (2014).
19. E. Moult, W. J. Choi, N. K. Waheed, M. Adhi, B. K. Lee, C. D. Lu, V. Jayaraman, B. Potsaid, P. J. Rosenfeld, J. S. Duker, and J. G. Fujimoto, "Ultrahigh-Speed Swept-Source OCT Angiography in Exudative AMD," Osli Retina **45**, 496-505 (2014).
20. B. Cense, H. C. Chen, B. H. Park, M. C. Pierce, and J. F. de Boer, "In vivo birefringence and thickness measurements of the human retinal nerve fiber layer using polarization-sensitive optical coherence tomography," J Biomed Opt **9**, 121-125 (2004).
21. S. Zotter, M. Pircher, E. Gotzinger, T. Torzicky, H. Yoshida, F. Hirose, S. Holzer, J. Kroisamer, C. Vass, U. Schmidt-Erfurth, and C. K. Hitzenberger, "Measuring Retinal Nerve Fiber Layer Birefringence, Retardation, and Thickness Using Wide-Field, High-Speed Polarization Sensitive Spectral Domain OCT," Invest Ophth Vis Sci **54**, 72-84 (2013).
22. R. N. Weinreb, A. W. Dreher, A. Coleman, H. Quigley, B. Shaw, and K. Reiter, "Histopathologic Validation of Fourier-Ellipsometry Measurements of Retinal Nerve-Fiber Layer Thickness," Arch Ophthalmol-Chic **108**, 557-560 (1990).
23. E. Gotzinger, M. Pircher, B. Baumann, C. Hirn, C. Vass, and C. K. Hitzenberger, "Retinal nerve fiber layer birefringence evaluated with polarization sensitive spectral domain OCT and scanning laser polarimetry: A comparison," Journal of Biophotonics **1**, 129-139 (2008).
24. M. Wolman and F. H. Kasten, "Polarized-Light Microscopy in the Study of the Molecular-Structure of Collagen and Reticulin," Histochemistry **85**, 41-49 (1986).
25. A. Viidik, "Functional properties of collagenous tissues," Int Rev Connect Tissue Res **6**, 127-215 (1973).
26. P. Roberts, M. Sugita, G. Deak, B. Baumann, S. Zotter, M. Pircher, S. Sacu, C. K. Hitzenberger, and U. Schmidt-Erfurth, "Automated Identification and Quantification of Subretinal Fibrosis in Neovascular Age-Related Macular Degeneration Using Polarization-Sensitive OCT," Invest Ophthalmol Vis Sci **57**, 1699-1705 (2016).
27. P. K. Roberts, S. Zotter, A. Montuoro, M. Pircher, B. Baumann, M. Ritter, C. K. Hitzenberger, and U. Schmidt-Erfurth, "Identification and Quantification of the Angiofibrotic Switch in Neovascular AMD," Invest Ophth Vis Sci **60**, 304-311 (2019).
28. M. R. Hee, D. Huang, E. A. Swanson, and J. G. Fujimoto, "Polarization-Sensitive Low-Coherence Reflectometer for Birefringence Characterization and Ranging," J Opt Soc Am B **9**, 903-908 (1992).
29. J. F. de Boer, T. E. Milner, M. J. van Gemert, and J. S. Nelson, "Two-dimensional birefringence imaging in biological tissue by polarization-sensitive optical coherence tomography," Opt Lett **22**, 934-936 (1997).
30. B. H. Park, M. C. Pierce, B. Cense, and J. F. de Boer, "Jones matrix analysis for a polarization-sensitive optical coherence tomography system using fiber-optic components," Opt Lett **29**, 2512-2514 (2004).

31. M. C. Pierce, B. H. Park, B. Cense, and J. F. de Boer, "Simultaneous intensity, birefringence, and flow measurements with high-speed fiber-based optical coherence tomography," Opt Lett **27**, 1534-1536 (2002).
32. B. H. Park, M. C. Pierce, B. Cense, S. H. Yun, M. Mujat, G. J. Tearney, B. E. Bouma, and J. F. de Boer, "Real-time fiber-based multi-functional spectral-domain optical coherence tomography at 1.3 mu m," Opt Express **13**, 3931-3944 (2005).
33. M. Villiger, E. Z. Zhang, S. K. Nadkarni, W. Y. Oh, B. J. Vakoc, and B. E. Bouma, "Spectral binning for mitigation of polarization mode dispersion artifacts in catheter-based optical frequency domain imaging," Opt Express **21**, 16353-16369 (2013).
34. E. Z. Zhang, W. Y. Oh, M. L. Villiger, L. Chen, B. E. Bouma, and B. J. Vakoc, "Numerical compensation of system polarization mode dispersion in polarization-sensitive optical coherence tomography," Opt Express **21**, 1163-1180 (2013).
35. B. Braaf, K. A. Vermeer, M. de Groot, K. V. Vienola, and J. F. de Boer, "Fiber-based polarization-sensitive OCT of the human retina with correction of system polarization distortions," Biomed Opt Express **5**, 2736-2758 (2014).
36. M. G. O. Gräfe, M. Gondre, and J. F. de Boer, "Precision analysis and optimization in phase decorrelation OCT velocimetry," Biomed Opt Express **10**, 1297-1314 (2019).
37. N. A. Nassif, B. Cense, B. H. Park, M. C. Pierce, S. H. Yun, B. E. Bouma, G. J. Tearney, T. C. Chen, and J. F. de Boer, "In vivo high-resolution video-rate spectral-domain optical coherence tomography of the human retina and optic nerve," Opt Express **12**, 367-376 (2004).
38. N. V. Iftimia, D. X. Hammer, C. E. Bigelow, D. I. Rosen, T. Ustun, A. A. Ferrante, D. Vu, and R. D. Ferguson, "Toward noninvasive measurement of blood hematocrit using spectral domain low coherence interferometry and retinal tracking," Opt Express **14**, 3377-3388 (2006).
39. J. Li and J. F. de Boer, "Coherent signal composition and global phase determination in signal multiplexed polarization sensitive optical coherence tomography," Opt Express **22**, 21382-21392 (2014).
40. M. Villiger, D. Lorenser, R. A. McLaughlin, B. C. Quirk, R. W. Kirk, B. E. Bouma, and D. D. Sampson, "Deep tissue volume imaging of birefringence through fibre-optic needle probes for the delineation of breast tumour," Sci Rep-Uk **6**(2016).
41. M. Yamanari, K. Ishii, S. Fukuda, Y. Lim, L. Duan, S. Makita, M. Miura, T. Oshika, and Y. Yasuno, "Optical Rheology of Porcine Sclera by Birefringence Imaging," Plos One **7**(2012).
42. F. Feroldi, J. Willemse, V. Davidoiu, M. G. O. Grafe, D. J. van Iperen, A. W. M. Goorsenberg, J. T. Annema, J. M. A. Daniels, P. I. Bonta, and J. F. de Boer, "In vivo multifunctional optical coherence tomography at the periphery of the lungs," Biomed Opt Express **10**, 3070-3091 (2019).
43. J. Willemse, M. G. O. Gräfe, J. A. van de Kreeke, F. Feroldi, F. D. Verbraak, and J. F. de Boer, "Optic axis uniformity as a metric to improve the contrast of birefringent structures and analyze the retinal nerve fiber layer in polarization-sensitive optical coherence tomography," Opt Lett **44**, 3893-3896 (2019).
44. E. Gotzinger, M. Pircher, W. Geitzenauer, C. Ahlers, B. Baumann, S. Michels, U. Schmidt-Erfurth, and C. K. Hitzenberger, "Retinal pigment epithelium segmentation by polarization sensitive optical coherence tomography," Opt Express **16**, 16410-16422 (2008).
45. B. Baumann, S. O. Baumann, T. Konegger, M. Pircher, E. Gotzinger, F. Schlanitz, C. Schutze, H. Sattmann, M. Litschauer, U. Schmidt-Erfurth, and C. K.

Hitzenberger, "Polarization sensitive optical coherence tomography of melanin provides intrinsic contrast based on depolarization," Biomed Opt Express **3**, 1670-1683 (2012).

46. S. Makita, Y. J. Hong, M. Miura, and Y. Yasuno, "Degree of polarization uniformity with high noise immunity using polarization-sensitive optical coherence tomography," Opt Lett **39**, 6783-6786 (2014).
47. M. E. H. Jaspers, F. Feroldi, M. Vlig, J. F. de Boer, and P. P. M. van Zuijlen, "In vivo polarization-sensitive optical coherence tomography of human burn scars: birefringence quantification and correspondence with histologically determined collagen density," J Biomed Opt **22**(2017).
48. D. J. Maitland and J. T. Walsh Jr, "Quantitative measurements of linear birefringence during heating of native collagen," Lasers in Surgery and Medicine **20**, 310-318 (1997).
49. M. Friedlander, "Fibrosis and diseases of the eye," J Clin Invest **117**, 576-586 (2007).
50. S. Fukuda, S. Beheregaray, D. Kasaragod, S. Hoshi, G. Kishino, K. Ishii, Y. Yasuno, and T. Oshika, "Noninvasive Evaluation of Phase Retardation in Blebs After Glaucoma Surgery Using Anterior Segment Polarization-Sensitive Optical Coherence Tomography," Invest Ophth Vis Sci **55**, 5200-5206 (2014).